PAPER

Check for updates

Efficient removal of heavy metals from polluted water with high selectivity for Hg(II) and Pb(II) by a 2-imino-4-thiobiuret chemically modified MIL-125 metal–organic framework†

Mina Shawky Adly,[ab] S. M. El-Dafrawy,[b] Amr A. Ibrahim, [iD][b] S. A. El-Hakam [iD] *[b] and M. Samy El-Shall [iD] *[a]

A highly porous adsorbent based on a metal–organic framework was successfully designed and applied as an innovative adsorbent in the solid phase for the heavy metal removal. MIL-125 was densely decorated by 2-imino-4-thiobiuret functional groups, which generated a green, rapid, and efficacious adsorbent for the uptake of Hg(II) and Pb(II) from aqueous solutions. ITB-MIL-125 showed a high adsorption affinity toward mercury(II) ions of 946.0 mg g^{-1} due to covalent bond formation with accessible sulfur-based functionality. Different factors were studied, such as the initial concentration, pH, contact time, and competitive ions, under same circumstances at the room temperature. Moreover, the experimental adsorption data were in excellent agreement with the Langmuir adsorption isotherm and pseudo-second order kinetics. At a high concentration of 100 ppm mixture of six metals, ITB-MIL-125 exhibited a high adsorption capacity, reaching more than 82% of Hg(II) compared to 62%, 30%, 2%, 1.9%, and 1.6% for Pb(II), Cu(II), Cd(II), Ni(II), and Zn(II), respectively.

1. Introduction

Heavy metal contamination in the environment is considered a true threat to water, soil, air, and the human body.[1] The recovery and elimination of toxic metal ions from wastewater is of concern with an increasing awareness towards the need for protecting nature. Mercury and lead are the most toxic species and can cause bioaccumulation in kidneys, brain, lung tissues, gastrointestinal tract, central nervous system, and reproductive system.[2,3] Toxic metals are released in nature due to fossil fuel combustion in power plants, ore processing, chemical and commercial industries, smelting, and geothermal eruptions.[4,5]

[a]Department of Chemistry, Virginia Commonwealth University, Richmond, VA 23284-2006, USA. E-mail: mselshal@vcu.edu
[b]Department of Chemistry, Faculty of Science, Mansoura University, Mansoura 35516, Egypt. E-mail: sehakam@mans.edu.eg

† Electronic supplementary information (ESI) available: Photograph of the adsorption experiment system (Fig. S1), Raman spectra of MIL-125 and ITB-MIL-125 (Fig. S2), N$_2$ adsorption–desorption isotherms and estimated BJH pore size distribution for MIL-125 and ITB-MIL-125 (Fig. S3), XPS survey spectrum of MIL-125 (a) and XPS high-resolution spectra of (b) C 1s, (c) Ti 2p and (d) O 1s (Fig. S4), comparison of adsorption capacities of MIL-125 and ITB-MIL-125 adsorbents for Hg(II), Pb(II), Cd(II) and As(v) (Fig. S5), effect of adsorbent mass on the removal efficiency of Hg(II), Pb(II), Cd(II) and As(v) (Fig. S6), ion exchange study at pH 6 for Hg(II) (Fig. S7), Langmuir adsorption isotherm (a) and pseudo-second order kinetic models (b) (Fig. S8), and XPS high-resolution spectra of N 1s (a) before and (b) after adsorption of Hg(II) ions (Fig. S9). See DOI: 10.1039/d1ra00927c

Estimations have illustrated that tens of millions of people at least have been affected by heavy metal toxicity in both industrialized and developed countries.[6] Over the years, many techniques, such as adsorption, ionic exchange, chemical deposition, solid–liquid phase extraction, coagulation, photocatalytic degradation, electrochemical, and membrane systems, have been developed.[7–12] However, most of these methods have limitations due to their slow sorption kinetics, low removal capacity, low stability, and non-reusability. Material science and chemistry face massive challenges to achieve a technique that meets high demands for high capacity, selectivity, efficiency, stability, and reusability.[13] The extraction of heavy metal ions from aqueous media by adsorption is considered one of the most efficacious methods, attributed to its low cost, ease of separation, simplicity, and high selectivity.[14,15] Thiol-based host materials, such as clay,[16] molecular sieves,[17] graphene oxide,[18] cellulose,[19,20] activated carbon (AC),[21] carbon nanotubes (CNTs),[22] silica gel,[23] zeolites,[24] and polymers,[25] have been designed as efficient synthetic adsorbents for the extraction of heavy metals.

Metal–organic frameworks (MOFs) are a new class of emerging porous materials that are attracting much attention in numerous prospective applications, such as gas storage, separation, heterogeneous catalysis, magnetism, drug delivery, fluorescence, and sensors.[26–34] MOFs show a highly significant role in environmental remediation as an efficient water-applicable adsorbent. Thiol-functionalized MOFs are attracting significant attention to mitigate the hazardous effects of

mercury and lead in the environment, due to their high surface area, extensive pore volume, and tunable pore size.[35] Besides these features, a unique property of MOFs is highly modifiable chelating sites created by π-columnar structures that facilitate the selective recognition and adsorption of different guest molecules.[13,29]

Herein, we developed a modified Ti(IV)-based metal–organic framework (MIL-125) containing Ti as metal nodes and 1,4-benzenedicarboxylic acid as an organic linker, which was connected by three-dimensional (3D) lattices functionalized by 2-imino-4-thiobiuret (ITB) to enhance the adsorption capacity toward noxious metals from solution. The designed adsorbent ITB-MIL-125 showed a highly chelating affinity to metal ions through introducing sulfur and amidoxime functional groups. This work presents an effective adsorbent for Hg(II) and Pb(II) and other toxic metals, such as Cd(II) and As(V), which demonstrated the removal of low and high concentration Hg(II) and Pb(II) from contaminated water. Samples were characterized and investigated by FT-IR, Raman, XRD, TEM, XPS, and BET techniques. Other parameters were also studied, like the solution pH, initial concentrations of metal ions, contact time, and competitive ions.

2. Experimental

2.1. Materials

All the materials were purchased from Sigma-Aldrich without further purifications, including titanium(IV) isopropoxide (97%), methanol, N,N-dimethylformamide (DMF), toluene, 1,4-benzenedicarboxylic acid, 2-imino-4-thiobiuret (99%). Stock solutions of heavy metals were made using $HgCl_2$, $Pb(NO_3)_2$, KH_2AsO_4, $Ni(NO_3)_2 \cdot 6H_2O$, $Cd(NO_3)_2 \cdot 4H_2O$, $Zn(NO_3)_2 \cdot 6H_2O$, and $Cu(NO_3)_2 \cdot 3H_2O$.

2.2. Synthesis of MIL-125

MIL-125 was prepared by the solvothermal method reported by Kim *et al.*[36] Here, 1,4-benzenedicarboxylic acid (15 mmol, 2.49 g) was dissolved in 50 mL of anhydrous DMF and methanol mixture (9 : 1, v/v). Titanium(IV) isopropoxide (9 mmol, 2.7 mL) was mixed into the mixture with stirring for 15 min. The reaction mixture was sealed in a 100 mL stainless steel Teflon tube and heated at 423 K for 16 h in a convection oven. The autoclave was allowed to cool to room temperature and then the obtained white precipitate was centrifuged at a speed of 5000 rpm and washed by DMF (3 times × 40 mL), followed by washing with diluted ethanol (3 times × 40 mL). Finally, the white solid was dried in a convection oven at 343 K overnight.

2.3. ITB grafting on the coordinatively unsaturated metal centers of MIL-125

The functionalization of Ti-based MOFs was prepared through the coordination bonds of unsaturated Ti metal centres and the amine groups in 2-imino-4-thiobiuret (ITB) because unsaturated sites or open metal sites were created from Ti octahedral clusters of MIL-125 after degassing.[37] MIL-125 was degassed at 423 K for 12 h. Next, 500 mg of MIL-125 was suspended in 30 mL

anhydrous toluene followed by the addition of 2.0 g of ITB to the reaction mixture, which was then refluxed under stirring at 363 K for 24 h. The solid was washed 3 times with diluted ethanol and dried in a convection oven at 343 K overnight.

2.4. Heavy metals extraction

The adsorption experiments of the heavy metals were carried out using 5 mL from the desired concentration in small vials with 0.005 g of the adsorbent at the optimum pH for each metal. The mixtures were allowed to be stirred using a magnetic stirrer at a speed of 800 rpm at room temperature. A photograph of the adsorption experiment is shown in Fig. S1 (ESI).† The mixtures were centrifuged to separate the metal-loaded adsorbents from the suspension and the volume of each aliquot was 100 μL. The remaining concentrations of metal ions in the supernatants were determined by inductively coupling plasma atomic emission spectroscopy (ICP-OES). The adsorption capacity (q_e) and the removal percentage were determined from the following eqn (1) and (2):

$$q_e = \frac{(C_o - C_e)\ V(\text{L})}{m(\text{g})} \qquad (1)$$

$$\%\ \text{removal} = \frac{C_o - C_e}{C_o} \times 100 \qquad (2)$$

where, q_e is the amount of metal ions adsorbed per mass of adsorbent (mg g^{-1}), C_o and C_e are the metal ion initial and equilibrium concentrations (mg L^{-1}), respectively, V is the volume of aqueous solution (L), and m is the mass of the adsorbent (g).

2.5. Kinetic studies

To study the effect of the contact time, 5 mL of x mg L^{-1} of metal ions were added to small glass vials with 0.005 g of adsorbent under stirring at 298 K. The aliquots were taken at time intervals of 5, 10, 15, 30, 45, 60, 75, 90, 120, 150, 180, 210, 240, 300, 360, 420, and 480 min. The aqueous solutions were centrifuged in micro Eppendorf tubes to separate the solid from the supernatant and then acidified by 2% HNO_3 prior to analysis. The optimum pH for adsorption of each metal ion was investigated by adjusting it using very dilute solutions of HNO_3 and NH_4OH. Also, the adsorbent dose effect was assessed with different masses of ITB-MIL-125 (0.2, 0.6, 1.0, 1.4, 1.8, and 2.2 g L^{-1}). The concentrations of metal ions in the supernatants for all experiments were measured by ICP-OES using eqn (2).

2.6. Characterization

The synthesized samples characterized by Raman and FT-IR spectra were collected on a Thermo Scientific DXR Smart Raman system using 532 nm excitation wavelength and a laser output power 10 mW, and Nicolet-Nexus 670 FT-IR spectrometer, respectively. The XRD patterns were obtained on an X'Pert Philips Materials Research diffractometer with a Cu target from 5° to 40°. TEM images obtained using the JEOL JEM-1230 microscope, and X-ray photoelectron spectroscopy (XPS) was performed using a Thermo Fisher Scientific ESCALAB 250 with a micro-focused monochromatic aluminium X-ray source (15

kV) and a double-focusing full 180° spherical sector electron analyzer. Multipack program version 9.8.0.19 was used for XPS analysis with the Shirley background and curve fitting by Gaussian–Lorentzian with 90% Gaussian. The heavy metal content in the supernatants was determined using a Varian Vista-MPX Inductively Coupled Plasma Optical Emission Spectrometer (ICP-OES) with Ar^+ ions plasma gas equipped with a charged-couple detector (CCD) with simultaneous detection. The N_2 adsorption–desorption isotherm analysis was carried out at 77 K using a Micromeritics 3Flex instrument.

3. Results and discussion

3.1. Design and characterization of MIL-125 and ITB-MIL-125

The functionalization of MIL-125 was confirmed by FT-IR spectra. Fig. 1(a), for pristine MIL-125, shows a broad band at 3340 cm^{-1}, which was assigned to –OH (stretching vibration), while the vibrational stretching frequencies of the framework (C–O–C) appeared at 1645 and 1388 cm^{-1}, confirming the terephthalic acid (dicarboxylic) linker in the MIL-125 structure.[38] The bands located at 1019 and 740 cm^{-1} are characteristic for benzene ring and bond between oxygen and metal (O–Ti–O), respectively.[39–41] Fig. 1(b) shows distinctive bands for the stretching vibration of N–H, which appear at 3271 and 3160 cm^{-1} attributed to the primary and secondary amine in ITB molecules. Furthermore, the bands at 1610 and 1075 cm^{-1} could be assigned to the N–H bending vibration of primary amine and C–S vibration, respectively. The main characteristic bands for MIL-125 could be noticed at the same time in the ITB-MIL-125 spectrum.

Raman analysis of MIL-125 and ITB-MIL-125 provided further confirmation of the framework structure. Relatively strong absorption bands could be observed at 430, 632, 700, 862, 1137, 1418, 1595, and 1626 cm^{-1} as shown in Fig. S2 (ESI).†[42] Both materials exhibited the same characteristic peaks with a slight shift in the case of ITB-MIL-125. This provides
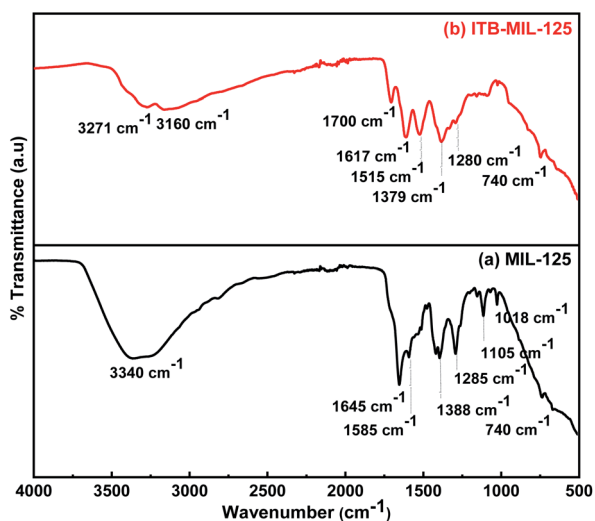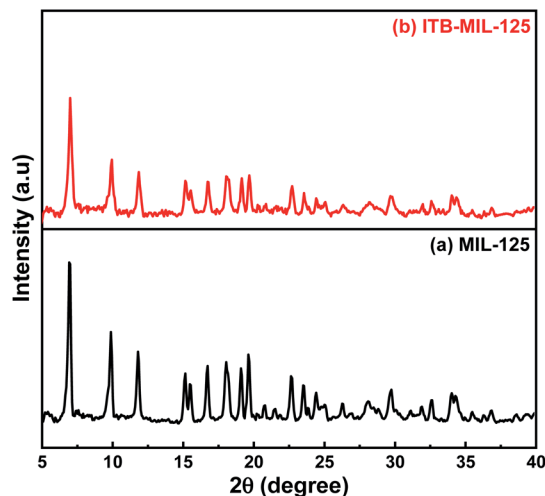

Fig. 2 XRD spectra of (a) MIL-125 and (b) ITB-MIL-125.

further evidence that MIL-125 was coordinated with ITB *via* chemical bonds, and was not just a simple mixture of the two samples and the chemical environment of Ti atoms was maintained.[39,43] The resonance-Raman band at 700 cm^{-1} was assigned to the octahedral coordination environment of the Ti framework species, *i.e.*, six oxygen atoms were connected to a single titanium atom. The bands at 1418 and 1626 cm^{-1} could be attributed to the bending and symmetric stretching of O–Ti–O octatomic ring species in the framework structure and the deposition of hydrocarbons, respectively.[44] The XRD patterns were used to identify the crystal structure of the samples as illustrated in Fig. 2. The 3D pores in the MIL-125 structure were formed by μ-OH corners sharing with TiO_6 octahedra interconnected to H_2BDC molecules.[44] Besides, the main characteristic diffraction peaks of MIL-125 were not changed by introducing ITB to the MIL-125 framework. Fig. S3 (ESI)† shows the N_2 adsorption–desorption isotherms of MIL-125 and ITB-MIL-125 at 77 K. The BET specific surface area (S_{BET}) was 1143.1 m^2 g^{-1} with a micropore volume and width of 0.36 cm^3 g^{-1} and 53.2 Å, respectively, for MIL-125. The S_{BET} was slightly decreased to 996.14 m^2 g^{-1} with a micropore volume and width of 0.28 cm^3 g^{-1} and 49.6 Å, respectively, compared to the as-prepared MIL-125 due to the attachment of 2-imino-4-thiobiuret to the MIL framework.

The elemental valance and chemical states of MIL-125 and ITB-MIL-125 could be obtained by the XPS measurements as illustrated in Fig. S4 (ESI)† and 3, respectively. The survey spectra of the samples showed the existence of C, Ti, O, N, and S elements. The C 1s spectrum for MIL-125 was deconvoluted into four peaks at 284.6, 286.2, 288.6, and 291.3 eV, assigned to C=C (sp^2), C–C (sp^3), C–O–Ti, and –COOR, respectively, as displayed in Fig. S4(b) (ESI).†

The C 1s spectrum for ITB-MIL-125 was split into five peaks fitted at 284.5, 285.5, 287.6, 288.7, and 291.8 eV, which could be ascribed to C=C, C–C, C–N, C–O–Ti, and –COOR groups, respectively. In the Ti 2p spectrum, two peaks at binding energies of 458.8 and 464.5 eV were fitted to Ti $2p_{3/2}$ and Ti $2p_{1/2}$,

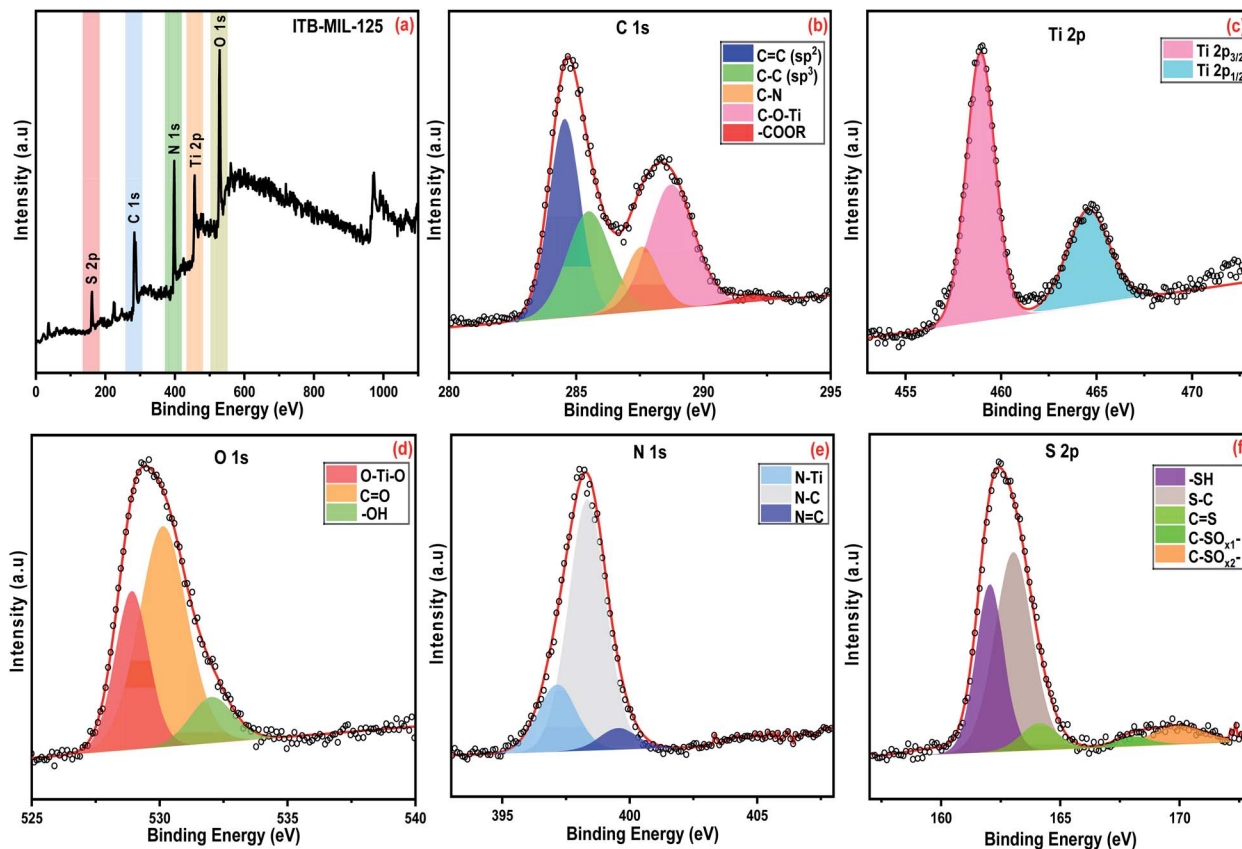Fig. 1 FT-IR patterns of (a) MIL-125 and (b) ITB-MIL-125.

Fig. 3 XPS survey spectrum of ITB-MIL-125 (a) and XPS high-resolution spectra of (b) C 1s, (c) Ti 2p, (d) O 1s, (e) N 1s and (f) S 2p.

respectively, implying that Ti(IV) existed in the titanium oxo-cluster. The O 1s spectrum was split into three peaks at 528.9, 530.2, and 532.1 eV, corresponding to O–Ti–O oxo-cluster, C=O, and –OH groups, respectively.[38,39] The XPS high-resolution analysis showed spectra attributed to N 1s and S 2p, which evidently showed the successful incorporation of amidoxime functional group on to the MIL-125 surface (Fig. 3(e and f)). The values of binding energies at 397.1, 398.3, and 399.6 eV were assigned to the deconvolution of N 1s to N–Ti, N–C, and N=C, respectively.[45,46] The S 2p spectrum was split into five peaks at binding energies of 162.0, 163.1, 164.4, 169.6, and 172.5 eV, attributed to S in –SH bonds, S in S–C bonds, S in S=C bonds, S in $C–SO_{x1}$ bonds, and S in $C–SO_{x2}$ bonds.[18,47] The peak at 397.1 eV was fitted to N–Ti, which provided evidence for the chelation between Ti in the MIL-125 framework and the nitrogen atoms in 2-imino-4-thiobiuret.

Fig. 4 shows TEM images for pristine MIL-125 before and after functionalization by 2-imino-4-thiobiuret. MIL-125 exhibited a regular decahedron morphology,[48] which displayed some variations in the crystalline morphology, which may be attributed to the addition of ITB to the dispersed MIL-125.

3.2. Adsorption capacity of heavy metals

The extraction of heavy metals from aqueous solutions by adsorption depends on the pH, so the initial pH of each metal ion was designed for optimal evaluation performance. Fig. 5(a)

shows the optimum pH for the maximum adsorption capacities of Hg(II), Pb(II), and Cd(II) was between 5.0–6.0. At a pH higher than 6.0, the metal ions precipitate due to the formation of metal hydroxides. The adsorption capacities of Hg(II), Pb(II), and Cd(II) were dimensioned by decreasing the pH values of the aqueous solutions. The removal efficiencies diminished due to protonation of the binding sites on the adsorbent surface, which increased the repulsive forces between the positive ions and adsorbent surface.[49] Furthermore, at lower pH, there was more competition between positive ions and H^+ for binding sites due to the high contamination of protons. The adsorption capacities increased at higher pH due to the strong attractive
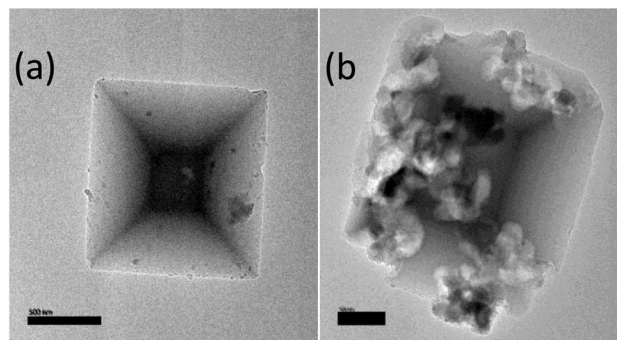

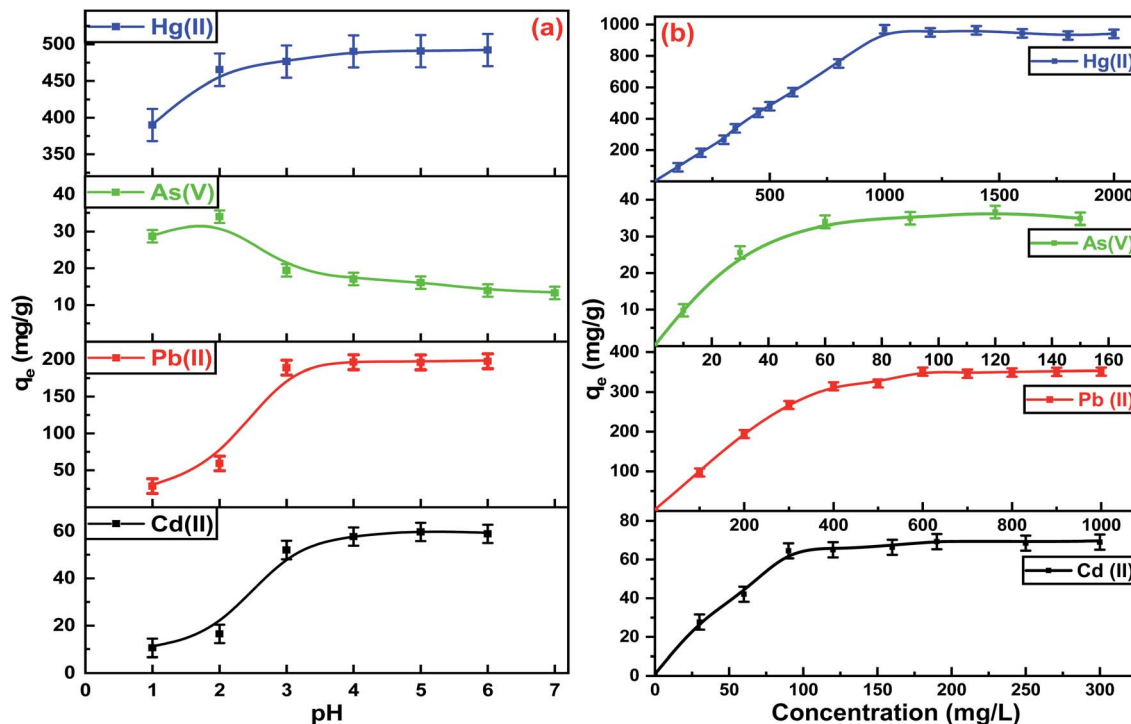**Fig. 4** TEM images of (a) MIL-125 and (b) ITB-MIL-125.

Fig. 5   (a) Effect of the initial pH on the adsorption capacities of Hg(ɪɪ), As(ᴠ), Pb(ɪɪ), and Cd(ɪɪ) from aqueous solutions [conditions: $C_o = 500$ mg L^{-1} Hg(ɪɪ), 60 mg L^{-1} As(ᴠ), 200 mg L^{-1} Pb(ɪɪ), 100 mg L^{-1} Cd(ɪɪ), adsorbent mass = 0.005 g, volume = 5 mL and T = 298 K]. (b) Effect of initial concentrations on the uptake of Hg(ɪɪ), As(ᴠ), Pb(ɪɪ), and Cd(ɪɪ) ions on ITB-MIL-125 [conditions: $C_o = 100–2000$ mg L^{-1} Hg(ɪɪ), 10–150 mg L^{-1} As(ᴠ), 100–1000 mg L^{-1} Pb(ɪɪ), and 30–300 mg L^{-1} Cd(ɪɪ); pH 6 for Hg(ɪɪ), Pb(ɪɪ), and Cd(ɪɪ) and pH 2 for As(ᴠ), adsorbent mass = 0.005 g, volume = 5 mL and T = 298 K].

forces between the binding sites on the ITB-MIL-125 surface that are negatively charged and the positive metal ions. In the case of As(ᴠ), the optimum pH was 2.0, which could be explained by the protonation of NH_2 groups on ITB-MIL-125 leading to q high electrostatic interaction between the anionic species $[H_2AsO_4]^-$ and adsorbent surface.[49] A series of various concentrations was prepared to study the influence of the initial concentrations at the optimum pH for each metal ion. As illustrated in Fig. 5(b), the adsorption capacity increased with increasing the concentration of heavy metal ions until reaching the state of equilibrium saturation. In the case of Hg(ɪɪ), it showed a range of 94.0–97.0% removal efficiencies for concentrations below 1000 mg L^{-1} with the maximum adsorption capacity reaching 946.0 $\pm$ 22.0 mg g^{-1} at pH 6. The high adsorption capacities were attributed to the formation of highly stable complexes resulting from the strong interaction between Hg(ɪɪ) and the low-lying empty 3d orbitals in sulfur atoms in the ligand, which act as strong binding sites.[50] The adsorption capacities for As(ᴠ) at pH 2, and Pb(ɪɪ) and Cd(ɪɪ) at pH 6 were 34.9 $\pm$ 1.7, 350.0 $\pm$ 4.2, and 68.9 $\pm$ 3.9 mg g^{-1}, respectively. To demonstrate the remarkable removal efficiencies for heavy metal ions of the functionalized MIL-125 compared to pristine MIL-125, the removal efficiencies of different metal ions were studied for MIL-125 under similar conditions for ITB-MIL-125, as shown in Fig. S5 (ESI).† The high adsorption capacities were attributed to the incorporation of multiple sulfur and nitrogen functional groups on the ITB-MIL-125 surface.

Fig. 6 shows the effect of contact time on the adsorption of metal ions from aqueous solutions by the ITB-MIL-125

adsorbent. ITB-MIL-125 showed an adsorption capacity for Hg(ɪɪ) and Pb(ɪɪ) at optimum pH 6 under low and high concentrations. It was clear that the removal efficiencies of Hg(ɪɪ) reached 100% and 95% for initial concentrations of 10 and 70 mg L^{-1} after 30 s and 10 min contact time, respectively. In the case of high concentrations, the contact time required to reach maximum removal increased to 60 and 75 min for initial concentrations of 500 and 1000 mg L^{-1}, respectively as shown in Fig. 6(a). The percentage removal reached a maximum after 5 min for 60 and 200 mg L^{-1} of Pb(ɪɪ) (Fig. 6(b)). At a longer contact time, the adsorption capacity for Hg(ɪɪ) remained constant and the optimum agitation time was maybe after 75 min. The adsorbent dose effect was studied in the adsorption of Hg(ɪɪ), Pb(ɪɪ), Cd(ɪɪ), and As(ᴠ), which exhibited high adsorption performances when increasing the dose from 0.2 to 2.2 g L^{-1}. The adsorption capacities increased from 6.1% and 21.9% to 99.1% and 99.0% for Hg(ɪɪ) and Pb(ɪɪ), respectively. In the cases of Cd(ɪɪ) and As(ᴠ), the removal percentages increased to 70.1% and 43.5%, respectively, using the dose of 2.2 g L^{-1} as displayed in Fig. S6 (ESI).† The remarkable enhancement of the adsorption capacities was attributed to the high availability of binding sites on the surface at a higher adsorbent dose. Experiments were conducted to evaluate the extent of ion exchange between Hg(ɪɪ) and Ti(ɪᴠ) in aqueous solution after 24 h. Fig. S7 (ESI)† shows the concentrations of Ti(ɪᴠ) in the four samples was less than 0.5 mg L^{-1}, which confirmed the adsorption of Hg(ɪɪ) without significant ion exchange with Ti(ɪᴠ).
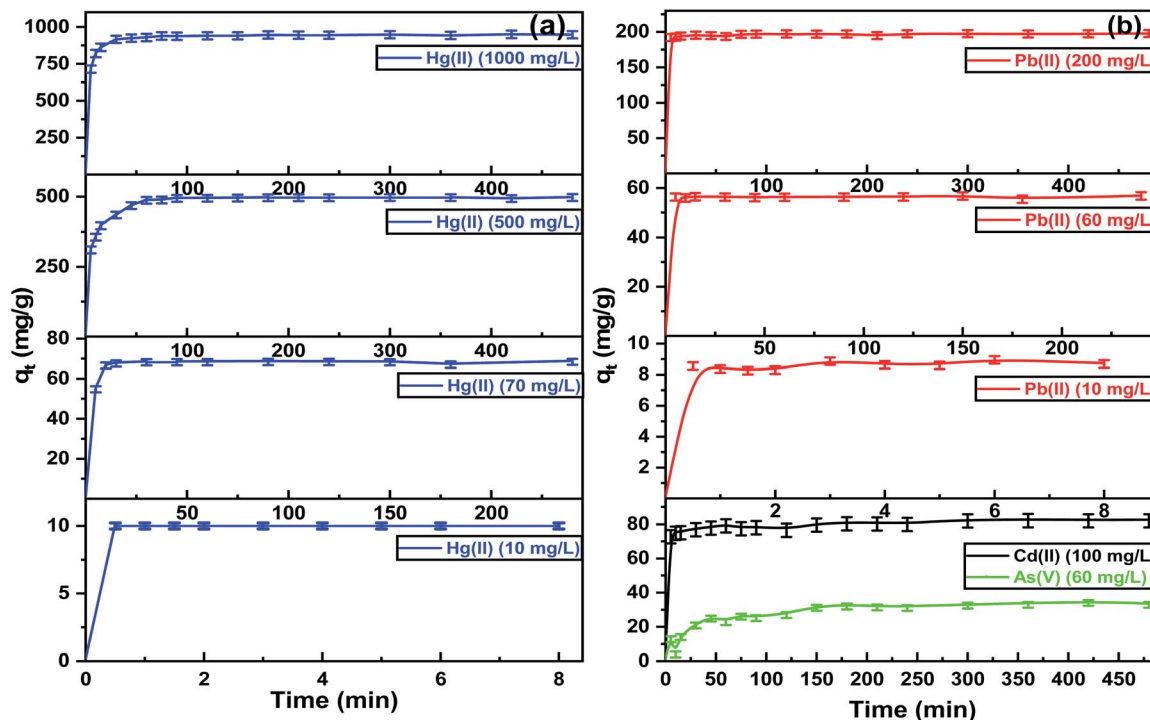
Fig. 6 Contact time studies for metal ions removal for (a) Hg(ɪɪ) [C_o = 10, 70, 500, and 1000 mg L^{-1}], (b) Pb(ɪɪ) [C_o = 10, 60, and 200 mg L^{-1}]. (c) Cd(ɪɪ) and As(v) [C_o = 100 and 60 mg L^{-1}, respectively]. Conditions: pH 6 for Hg(ɪɪ), Pb(ɪɪ), and Cd(ɪɪ), pH 2 for As(v), mass adsorbent = 0.005 g, volume = 5 mL and T = 298 K.

3.3. Adsorption isotherm

In general, the adsorption isotherm is an equilibrium relation used to describe the interaction between metal ions and the binding sites distributed on a solid surface and therefore it is a certain way of optimizing the use of adsorbents. The Langmuir model is used to study the adsorption isotherm by applying the following linear relation (eqn (3)):

$$\frac{1}{q_e} = \frac{1}{bq_m} + \frac{1}{q_m}C_e \qquad (3)$$

where; C_e is the solute concentration at equilibrium (mg L^{-1}), q_e is the quantity of solute adsorbed per mass of adsorbent (mg g^{-1}), b is the Langmuir constant related to the sorption affinity between the ITB-MIL-125 and aqueous solution (L mg^{-1}), and q_m is the Langmuir monolayer adsorption capacity (mg g^{-1}). This model assumes a one-on-one manner, whereby each adsorptive site can attract only one metal ion. The dimensionless equilibrium (R_L) is an important and characteristic parameter of the Langmuir adsorption isotherm, which is given as:

$$R_L = \frac{1}{1 + bC_o} \qquad (4)$$

On the other hand, the Freundlich isotherm model is assumed to describe the adsorption on the heterogeneous surface of the adsorbent, which can be expressed by the following linear relation (eqn (5)):

$$\log q_e = \log K_f + \frac{1}{n}\log C_e \qquad (5)$$

where, n and K_f are parameters corresponding to the adsorption intensity and capacity, respectively. Table 1 lists the Langmuir and Freundlich constants obtained by the linear fitting process. The correlation coefficients obtained by applying the Langmuir equation were higher than from the Freundlich equation; therefore, the Langmuir model (as shown in Fig. S8(a) (ESI)†) showed better fitting than the Freundlich, which indicated the adsorption of metal ions on the surface of ITB-MIL-125 was restricted to monolayer formation and there were no interactions with each other.[22,51]

3.4. Adsorption kinetics on the ITB-MIL-125 surface

Two kinetic models, namely the pseudo-first order and pseudo-second order equations, were examined to suggest the proposed mechanism for the adsorption kinetics.[52,53]

Pseudo-first order equation:

$$\log(q_e - q_t) = \log q_e - \frac{k_1 t}{2.303} \qquad (6)$$

Pseudo-second order equation:

$$\frac{t}{q_t} = \frac{1}{k_2 q_e^2} + \frac{1}{q_e}t \qquad (7)$$

where, k_1 (min^{-1}) and k_2 (g mol^{-1} min^{-1}) are rate constants corresponding to the pseudo-first and pseudo-second orders, respectively, and q_e and q_t (mg g^{-1}) represent the amounts of metal ions adsorbed at equilibrium and at time = t, respectively. The fitting validity of these models was checked by linear

Table 1 Langmuir and Freundlich adsorption isotherms constants for the adsorption of Hg(II), Pb(II), Cd(II), and As(V) on the ITB-MIL-125 adsorbent

| Metal ion | C_o (mg L^{-1}) | q_m, exp (mg g^{-1}) | Langmuir isotherm | | | | Freundlich isotherm | | |
			R_L	b (L mg^{-1})	q_m, calcd (mg g^{-1})	R^2	K_f ((mg g^{-1})/(mg mL^{-1})$^{1/n}$)	n	R^2
Hg(II)	2000	946.0	0.0112	0.044	970.0	0.9963	3.3×10^{-5}	0.43450	0.71475
Pb(II)	1000	350.0	0.0095	0.104	355.0	0.9996	5.5×10^{-9}	0.23792	0.80878
Cd(II)	300	68.9	0.0063	0.526	69.4	0.9996	7.1×10^{-6}	0.26547	0.29326
As(V)	150	34.9	0.0062	1.064	35.2	0.9998	5.7×10^{-6}	0.22198	0.89248

Table 2 Kinetic parameters of the pseudo-first and pseudo-second orders for the adsorption of Hg(II), Pb(II), Cd(II), and As(V) on the ITB-MIL-125 adsorbent

| Metal ion | C_o (mg L^{-1}) | q_e, exp (mg g^{-1}) | Pseudo-first order model | | | | Pseudo-second order model | | |
			q_e, calcd (mg g^{-1})	k_1 (min^{-1})	R^2		q_e, calcd (mg g^{-1})	k_2 (L mol^{-1} min^{-1})	R^2
Hg(II)	500	496.9	35.3	0.0129	0.55753		500.0	0.0008	0.99991
Pb(II)	200	193.5	3.1	0.0073	0.51665		197.6	0.0089	0.99998
Cd(II)	100	79.2	6.9	0.0064	0.75211		82.3	0.0034	0.99972
As(V)	60	35.3	15.1	0.0070	0.86799		34.7	0.0013	0.99711

plotting $\log(q_e - q_t)$ vs. t and t/q_t vs. t for pseudo-first and pseudo-second orders, respectively. Fig. S8(b) (ESI)† shows the excellent fits of the adsorption kinetics to the pseudo-second order model. In Table 2, the values of R^2 are in excellent agreement with the pseudo-second order, which describes the adsorption of metal ions on the ITB-MIL-125 surface and the rate-determining step governed by the chemisorption process.[50,54]

3.5. Competitive ions adsorption on ITB-MIL-125

It was important to investigate the adsorption performance in the presence of co-ions like Pb(II), Cd(II), Zn(II), Cu(II), and Ni(II) on the ITB-MIL-125 adsorbent. These ions are considered a competitive species during the uptake of Hg(II) and Pb(II) in surface water sources.[55] To study the influence of competitive ions, the experimental approaches were conducted under equal concentrations of Hg(II) and Pb(II) with the co-ions. The affinity of the adsorbent toward the co-ions could be ordered according to the following sequence: Hg(II) > Pb(II) > Cu(II) > Cd(II) > Ni(II) > Zn(II) (Fig. 7). The affinities of ITB-MIL-125 toward Hg(II) and Pb(II) uptake were slightly affected by the presence of the other metals that existed together in the same solution. At high concentration of 100 ppm, ITB-MIL-125 exhibited more than 82% removal efficiency of Hg(II) compared to 62%, 30%, 2%, 1.9%, and 1.6% for Pb(II), Cu(II), Cd(II), Ni(II), and Zn(II), respectively.

3.6. Mechanism of Hg(II) uptake by the ITB-MIL-125 adsorbent

A facile strategy was investigated to fabricate 2-imino-4-thiobiuret-grafted MIL-125 by a postsynthetic modification technique after vacuum treatment. The functional groups in ITB generate highly chelating binding sites, which coordinate

well with heavy metals. The successful synthesis of ITB-MIL-125 was confirmed with different characterization techniques, as mentioned above. XPS spectrum of ITB-MIL-125 obtained after the adsorption of Hg(II) showed two peaks at 100.0 and 104.1 eV, assigned to Hg 4f$_{7/2}$ and Hg 4f$_{5/2}$, respectively, with a spin-orbital splitting of 4.1 eV.[47] The higher shift of binding energies values compared to free Hg(II) could be attributed to the formation of complexes by chelation with the sulfur and nitrogen functional groups in ITB. The formation of complexes was confirmed by the high-resolution S 2p spectra before and after the adsorption of Hg(II) ions as displayed in Fig. 8. The synthetic material incorporating functional groups like sulfur and nitrogen exhibited a high binding affinity to mercury and lead ions. Fig. S9 (ESI)† displays the high-resolution XPS
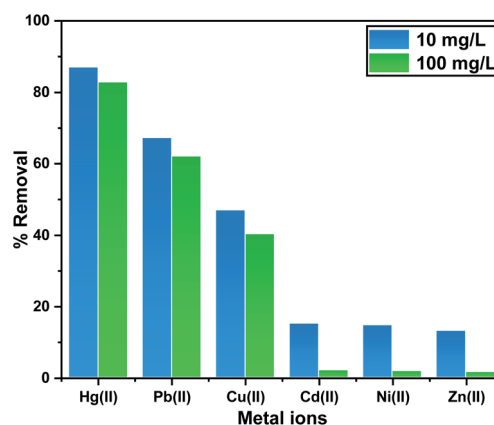

Fig. 7 Adsorption efficiencies of metal ions from aqueous solution containing Hg(II), Pb(II), Cd(II), Ni(II), Cu(II) and Zn(II) using ITB-MIL-125 adsorbent [conditions: C_o = 10 and 100 mg L^{-1}, adsorbent mass = 0.005 g, pH 6, volume = 5 mL and T = 298 K].
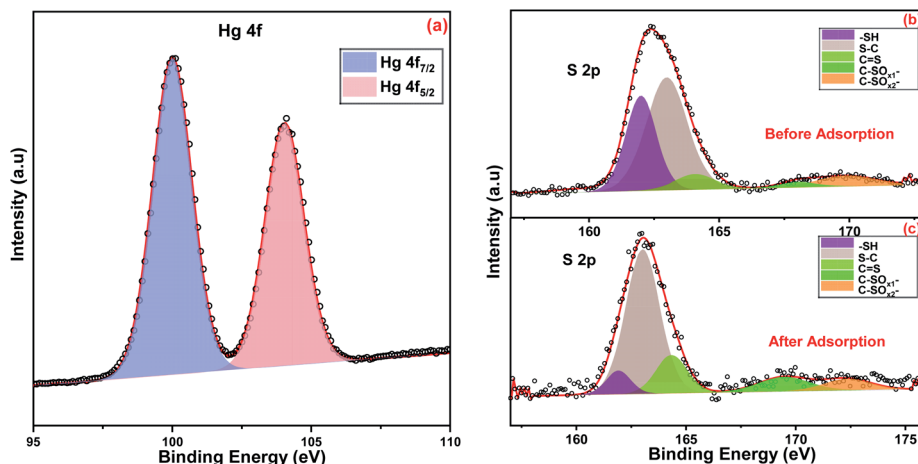
Fig. 8 XPS high-resolution of (a) Hg 4f, (b) S 2p before adsorption and (c) S 2p after adsorption.

Table 3 Comparison of the adsorption capacities of different adsorbents for Hg(II)

Adsorbent	q_e (mg g^{-1})	Ref.
MPTS–CNTs/Fe$_3$O$_4$ nanocomposites	65.52	22
Cyst-prGO	169.0	55
SWCNTs/Fe$_3$O$_4$@PDA	249.07	57
Magnetic PPy–GO	400.0	58
UIO-66-SH	785.0	59
NENU-401	596.6	60
ZrSulf	824.0	61
TMU-31	476.0	62
Pt NP@UiO-66-NH$_2$	243.9	63
MOF-808/AO	383.8	64
JUC-62	836.7	65
ITB-MIL-125	946.0	This work

spectrum of N 1s after adsorption of mercury, which shows a shift to higher binding energies, which may be attributed to the formation of complexes with nitrogen functional groups on the ITB-MIL-125 surface. After Hg adsorption, a new peak appeared at 404.8 eV assigned to N–O, which indicated both sulfur and nitrogen functional groups were coordinated to Hg(II) ions.[49,56]

3.7. Comparison studies of ITB-MIL-125 with other adsorbents

Table 3 shows the efficiency of ITB-MIL-125 for the adsorption of mercury ions from an aqueous solution compared to other adsorbents in the literature. The functionalized MIL-125 with 2-imino-4-thiobiuret showed a higher adsorption capacity compared to other adsorbents and functionalized MOFs.

4. Conclusion

In this work, MIL-125 functionalized with 2-imino-4-thiobiuret including different moieties, like nitrogen and sulfur, was successfully prepared and investigated as a high-performing adsorbent for Hg(II) and Pb(II). The bimolecular interactions between the binding sites on the adsorbent surface and adsorbate molecules involved the sharing of electrons due to the strong chelating effects of the sulfur and nitrogen functional groups within the ITB-NIL-125 adsorbent. The high surface area and a wide distribution of adsorptive sites for specific binding, which are important for designing high-performance adsorbents, were confirmed with various characterization methods. The data obtained from the adsorption experiments of heavy metals showed a high adsorption capacity, stability, and selectivity toward mercury at low and high concentrations, with a maximum adsorption capacity of 946.0 ± 22.0 mg g^{-1} at pH 6. High uptake values for other metal ions, like As(v) at pH 2, and Pb(II) and Cd(II) at pH 6, were reported with sorption capacities of 34.9 ± 1.7, 350.0 ± 4.2, and 68.9 ± 3.9 mg g^{-1}, respectively. The removal of metal ions using ITB-MIL-125 exhibited excellent fitting with the Langmuir adsorption isotherm and pseudo-second order kinetic models. The functionalized MIL frameworks showed a high adsorption performance for other heavy metals, like Pb(II), Cd(II), and As(v).

Conflicts of interest

There are no conflicts to declare.

Acknowledgements

References

1 F. Ke, L. G. Qiu, Y. P. Yuan, F. M. Peng, X. Jiang, A. J. Xie, Y. H. Shen and J. F. Zhu, Thiol-functionalization of metal-organic framework by a facile coordination-based

postsynthetic strategy and enhanced removal of Hg^{2+} from water, *J. Hazard. Mater.*, 2011, **196**, 36–43.

2 S. A. Hashemi, S. M. Mousavi and S. Ramakrishna, Effective removal of mercury, arsenic and lead from aqueous media using polyaniline-Fe_3O_4-silver diethyldithiocarbamate nanostructures, *J. Cleaner Prod.*, 2019, **239**, 118023.

3 T. Pasinszki, M. Krebsz, D. Chand, L. Kótai, Z. Homonnay, I. E. Sajó and T. Váczi, Carbon microspheres decorated with iron sulfide nanoparticles for mercury(II) removal from water, *J. Mater. Sci.*, 2019, **55**, 1425–1435.

4 Z. Zhou, X. Liu, C. Li, X. Elvis Cao and M. Xu, Seawater-assisted synthesis of MnCe/zeolite-13X for removing elemental mercury from coal-fired flue gas, *Fuel*, 2020, **262**, 116605.

5 H. Wu, J. Sun, C. Zhou and H. Yang, Effect of additives on stabilization and inhibition of mercury re-emission in simulated desulphurization slurry, *J. Environ. Sci. Technol.*, 2019, **16**, 7705–7714.

6 C. J. Vorosmarty, P. B. McIntyre, M. O. Gessner, D. Dudgeon, A. Prusevich, P. Green, S. Glidden, S. E. Bunn, C. A. Sullivan, C. R. Liermann and P. M. Davies, Global threats to human water security and river biodiversity, *Nature*, 2010, **467**, 555–561.

7 K. Gai, A. Avellan, T. P. Hoelen, F. Lopez-Linares, E. S. Hatakeyama and G. V. Lowry, Impact of mercury speciation on its removal from water by activated carbon and organoclay, *Water Res.*, 2019, **157**, 600–609.

8 E. Carvajal-Florez and C.-G. Santiago-Alonso, Technologies applicable to the removal of heavy metals from landfill leachate, *Environ. Sci. Pollut. Res.*, 2019, **26**, 15725–15753.

9 S. Rodriguez-Mozaz, M. J. de Alda and D. Barcelo, Monitoring of estrogens, pesticides and bisphenol A in natural waters and drinking water treatment plants by solid-phase extraction-liquid chromatography-mass spectrometry, *J. Chromatogr. A*, 2004, **1045**, 85–92.

10 A. Lerch, S. Panglisch, P. Buchta, Y. Tomita, H. Yonekawa, K. Hattori and R. Gimbel, Direct river water treatment using coagulation/ceramic membrane microfiltration, *Desalination*, 2005, **179**, 41–50.

11 M. S. Adly, S. M. El-Dafrawy and S. A. El-Hakam, Application of nanostructured graphene oxide/titanium dioxide composites for photocatalytic degradation of rhodamine B and acid green 25 dyes, *J. Mater. Res. Technol.*, 2019, **8**, 5610–5622.

12 B. P. Chaplin, Critical review of electrochemical advanced oxidation processes for water treatment applications, *Environ. Sci.: Processes Impacts*, 2014, **16**, 1182–1203.

13 C. Wang, C. He, Y.-H. Luo, S. Su, J.-Y. Wang, D.-L. Hong, X.-T. He, C. Chen and B.-W. Sun, Efficient mercury chloride capture by ultrathin 2D metal-organic framework nanosheets, *Chem. Eng. J.*, 2020, **379**, 122337.

14 Q. R. Fang, D. Q. Yuan, J. Sculley, J. R. Li, Z. B. Han and H. C. Zhou, Functional mesoporous metal-organic frameworks for the capture of heavy metal ions and size-selective catalysis, *Inorg. Chem.*, 2010, **49**, 11637–11642.

15 S. J. Tesh and T. B. Scott, Nano-composites for water remediation: a review, *Adv. Mater.*, 2014, **26**, 6056–6068.

16 R. Celis, M. C. Hermosin and J. Cornejo, Heavy Metal Adsorption by Functionalized Clays, *Environ. Sci. Technol.*, 2000, **34**, 4593–4599.

17 V. Hernández-Morales, R. Nava, Y. J. Acosta-Silva, S. A. Macías-Sánchez, J. J. Pérez-Bueno and B. Pawelec, Adsorption of lead(II) on SBA-15 mesoporous molecular sieve functionalized with –NH_2 groups, *Microporous Mesoporous Mater.*, 2012, **160**, 133–142.

18 F. S. Awad, K. M. AbouZeid, W. M. A. El-Maaty, A. M. El-Wakil and M. S. El-Shall, Efficient Removal of Heavy Metals from Polluted Water with High Selectivity for Mercury(II) by 2-Imino-4-thiobiuret-Partially Reduced Graphene Oxide (IT-PRGO), *ACS Appl. Mater. Interfaces*, 2017, **9**, 34230–34242.

19 M. Algarra, M. I. Vázquez, B. Alonso, C. M. Casado, J. Casado and J. Benavente, Characterization of an engineered cellulose based membrane by thiol dendrimer for heavy metals removal, *Chem. Eng. J.*, 2014, **253**, 472–477.

20 Z. Wu, Z. Cheng and W. Ma, Adsorption of Pb(II) from glucose solution on thiol-functionalized cellulosic biomass, *Bioresour. Technol.*, 2012, **104**, 807–809.

21 J. Li, X. Xing, J. Li, M. Shi, A. Lin, C. Xu, J. Zheng and R. Li, Preparation of thiol-functionalized activated carbon from sewage sludge with coal blending for heavy metal removal from contaminated water, *Environ. Pollut.*, 2018, **234**, 677–683.

22 C. Zhang, J. Sui, J. Li, Y. Tang and W. Cai, Efficient removal of heavy metal ions by thiol-functionalized superparamagnetic carbon nanotubes, *Chem. Eng. J.*, 2012, **210**, 45–52.

23 R. Rostamian, M. Najafi and A. A. Rafati, Synthesis and characterization of thiol-functionalized silica nano hollow sphere as a novel adsorbent for removal of poisonous heavy metal ions from water: kinetics, isotherms and error analysis, *Chem. Eng. J.*, 2011, **171**, 1004–1011.

24 X. Y. Zhang, Q. C. Wang, S. Q. Zhang, X. J. Sun and Z. S. Zhang, Stabilization/solidification (S/S) of mercury-contaminated hazardous wastes using thiol-functionalized zeolite and Portland cement, *J. Hazard. Mater.*, 2009, **168**, 1575–1580.

25 B. Aguila, Q. Sun, J. A. Perman, L. D. Earl, C. W. Abney, R. Elzein, R. Schlaf and S. Ma, Efficient Mercury Capture Using Functionalized Porous Organic Polymer, *Adv. Mater.*, 2017, **29**, 1700665.

26 N. L. Rosi, J. Eckert, M. Eddaoudi, D. T. Vodak, J. Kim, M. O, Keeffe and O. M. Yaghi, Hydrogen storage in microporous metal-organic frameworks, *Science*, 2003, **300**, 1127–1129.

27 J. L. Rowsell, A. R. Millward, K. S. Park and O. M. Yaghi, Hydrogen sorption in functionalized metal-organic frameworks, *J. Am. Chem. Soc.*, 2004, **126**, 5666–5667.

28 S. Basu, A. Cano-Odena and I. F. J. Vankelecom, MOF-containing mixed-matrix membranes for CO_2/CH_4 and CO_2/N_2 binary gas mixture separations, *Sep. Purif. Technol.*, 2011, **81**, 31–40.

29 C. D. Wu and M. Zhao, Incorporation of Molecular Catalysts in Metal-Organic Frameworks for Highly Efficient Heterogeneous Catalysis, *Adv. Mater.*, 2017, **29**, 1605446.

30 R. F. D, Vries, N. Snejko, M. Iglesias, E. Gutiérrez-Puebla and M. A. Monge, Ln-MOF Pseudo-Merohedral Twinned Crystalline Family as Solvent-Free Heterogeneous Catalysts, *Cryst. Growth Des.*, 2014, **14**, 2516–2521.

31 Y. Li, M. Xue, L. Guo, L. Huang, S. Chen and S. Qiu, A unique (4,12)-connected lanthanide metal-organic framework based on tetranuclear building blocks: topological analysis, fluorescence and magnetism properties, *Inorg. Chem. Commun.*, 2013, **28**, 25–30.

32 M. A. Nasalevich, R. Becker, E. V. Ramos-Fernandez, S. Castellanos, S. L. Veber, M. V. Fedin, F. Kapteijn, J. N. H. Reek, J. I. van der Vlugt and J. Gascon, Co@NH$_2$-MIL-125(Ti): cobaloxime-derived metal–organic framework-based composite for light-driven H$_2$ production, *Energy Environ. Sci.*, 2015, **8**, 364–375.

33 M. A. Lucena, M. F. Oliveira, A. M. Arouca, M. Talhavini, E. A. Ferreira, S. Alves Jr, F. H. Veiga-Souza and I. T. Weber, Application of the Metal-Organic Framework [Eu(BTC)] as a Luminescent Marker for Gunshot Residues: A Synthesis, Characterization, and Toxicity Study, *ACS Appl. Mater. Interfaces*, 2017, **9**, 4684–4691.

34 X. Mi, D. Sheng, Y. Yu, Y. Wang, L. Zhao, J. Lu, Y. Li, D. Li, J. Dou, J. Duan and S. Wang, Tunable Light Emission and Multiresponsive Luminescent Sensitivies in Aqueous Solutions of Two Series of Lanthanide Metal-Organic Frameworks Based on Structurally Related Ligands, *ACS Appl. Mater. Interfaces*, 2019, **11**, 7914–7926.

35 J. E. Efome, D. Rana, T. Matsuura and C. Q. Lan, Metal–organic frameworks supported on nanofibers to remove heavy metals, *J. Mater. Chem. A*, 2018, **6**, 4550–4555.

36 S.-N. Kim, J. Kim, H.-Y. Kim, H.-Y. Cho and W.-S. Ahn, Adsorption/catalytic properties of MIL-125 and NH$_2$-MIL-125, *Catal. Today*, 2013, **204**, 85–93.

37 X. Luo, L. Ding and J. Luo, Adsorptive Removal of Pb(II) Ions from Aqueous Samples with Amino-Functionalization of Metal–Organic Frameworks MIL-101(Cr), *J. Chem. Eng. Data*, 2015, **60**, 1732–1743.

38 Z. Yang, X. Xu, X. Liang, C. Lei, Y. Cui, W. Wu, Y. Yang, Z. Zhang and Z. Lei, Construction of heterostructured MIL-125/Ag/g-C$_3$N$_4$ nanocomposite as an efficient bifunctional visible light photocatalyst for the organic oxidation and reduction reactions, *Appl. Catal., B*, 2017, **205**, 42–54.

39 Z. Li, G. Che, W. Jiang, L. Liu and H. Wang, Visible-light-driven CQDs@MIL-125(Ti) nanocomposite photocatalyst with enhanced photocatalytic activity for the degradation of tetracycline, *RSC Adv.*, 2019, **9**, 33238–33245.

40 S. Kampouri, T. N. Nguyen, M. Spodaryk, R. G. Palgrave, A. Züttel, B. Smit and K. C. Stylianou, Concurrent Photocatalytic Hydrogen Generation and Dye Degradation Using MIL-125-NH$_2$ under Visible Light Irradiation, *Adv. Funct. Mater.*, 2018, **28**, 1806368.

41 H. E. Emam, H. B. Ahmed, E. Gomaa, M. H. Helal and R. M. Abdelhameed, Doping of silver vanadate and silver tungstate nanoparticles for enhancement the photocatalytic activity of MIL-125-NH$_2$ in dye degradation, *J. Photochem. Photobiol., A*, 2019, **383**, 118023.

42 Y. Fu, D. Sun, Y. Chen, R. Huang, Z. Ding, X. Fu and Z. Li, An amine-functionalized titanium metal-organic framework photocatalyst with visible-light-induced activity for CO$_2$ reduction, *Angew. Chem., Int. Ed.*, 2012, **51**, 3364–3367.

43 Z. Sun, J. Guo, S. Zhu, L. Mao, J. Ma and D. Zhang, A high-performance Bi$_2$WO$_6$-graphene photocatalyst for visible light-induced H$_2$ and O$_2$ generation, *Nanoscale*, 2014, **6**, 2186–2193.

44 S. Hu, M. Liu, K. Li, Y. Zuo, A. Zhang, C. Song, G. Zhang and X. Guo, Solvothermal synthesis of NH$_2$-MIL-125(Ti) from circular plate to octahedron, *CrystEngComm*, 2014, **16**, 9645–9650.

45 D. Jaeger and J. Patscheider, A complete and self-consistent evaluation of XPS spectra of TiN, *J. Electron Spectrosc. Relat. Phenom.*, 2012, **185**, 523–534.

46 H. Dai, X. Gao, E. Liu, Y. Yang, W. Hou, L. Kang, J. Fan and X. Hu, Synthesis and characterization of graphitic carbon nitride sub-microspheres using microwave method under mild condition, *Diamond Relat. Mater.*, 2013, **38**, 109–117.

47 V. Chandra and K. S. Kim, Highly selective adsorption of Hg^{2+} by a polypyrrole-reduced graphene oxide composite, *Chem. Commun.*, 2011, **47**, 3942–3944.

48 M. Sohail, H. Kim and T. W. Kim, Enhanced photocatalytic performance of a Ti-based metal-organic framework for hydrogen production: hybridization with ZnCr-LDH nanosheets, *Sci. Rep.*, 2019, **9**, 7584.

49 A. M. Bakry, F. S. Awad, J. A. Bobb and M. S. El-Shall, Multifunctional Binding Sites on Nitrogen-Doped Carboxylated Porous Carbon for Highly Efficient Adsorption of Pb(II), Hg(II), and Cr(VI) Ions, *ACS Omega*, 2020, **5**, 33090–33100.

50 C. Xiong, Q. Jia, X. Chen, G. Wang and C. Yao, Optimization of Polyacrylonitrile-2-aminothiazole Resin Synthesis, Characterization, and Its Adsorption Performance and Mechanism for Removal of Hg(II) from Aqueous Solutions, *Ind. Eng. Chem. Res.*, 2013, **52**, 4978–4986.

51 L. Ai, C. Zhang and L. Meng, Adsorption of Methyl Orange from Aqueous Solution on Hydrothermal Synthesized Mg–Al Layered Double Hydroxide, *J. Chem. Eng. Data*, 2011, **56**, 4217–4225.

52 A. A. Alqadami, M. Naushad, Z. A. Alothman and A. A. Ghfar, Novel Metal-Organic Framework (MOF) Based Composite Material for the Sequestration of U(VI) and Th(IV) Metal Ions from Aqueous Environment, *ACS Appl. Mater. Interfaces*, 2017, **9**, 36026–36037.

53 E. E. Khozemy, S. M. Nasef and T. M. Mohamed, Radiation Synthesis of Superabsorbent Hydrogel (Wheat Flour/Acrylamide) for Removal of Mercury and Lead Ions from Waste Solutions, *J. Inorg. Organomet. Polym. Mater.*, 2019, **30**, 1669–1685.

54 B. Saha, S. Das, J. Saikia and G. Das, Preferential and Enhanced Adsorption of Different Dyes on Iron Oxide Nanoparticles: A Comparative Study, *J. Phys. Chem. C*, 2011, **115**, 8024–8033.

55 P. L. Yap, S. Kabiri, D. N. H. Tran and D. Losic, Multifunctional Binding Chemistry on Modified Graphene

Composite for Selective and Highly Efficient Adsorption of Mercury, *ACS Appl. Mater. Interfaces*, 2019, **11**, 6350–6362.

56 H. Cui, Y. Qian, Q. Li, Q. Zhang and J. Zhai, Adsorption of aqueous Hg(II) by a polyaniline/attapulgite composite, *Chem. Eng. J.*, 2012, **211–212**, 216–223.

57 S. S. Ghasemi, M. Hadavifar, B. Maleki and E. Mohammadnia, Adsorption of mercury ions from synthetic aqueous solution using polydopamine decorated SWCNTs, *J. Water Process. Eng.*, 2019, **32**, 100965.

58 C. Zhou, H. Zhu, Q. Wang, J. Wang, J. Cheng, Y. Guo, X. Zhou and R. Bai, Adsorption of mercury(II) with an Fe₃O₄ magnetic polypyrrole–graphene oxide nanocomposite, *RSC Adv.*, 2017, **7**, 18466–18479.

59 J. Li, Y. Liu, Y. Ai, A. Alsaedi, T. Hayat and X. Wang, Combined experimental and theoretical investigation on selective removal of mercury ions by metal organic frameworks modified with thiol groups, *Chem. Eng. J.*, 2018, **354**, 790–801.

60 S. Y. Jiang, W. W. He, S. L. Li, Z. M. Su and Y. Q. Lan, Introduction of Molecular Building Blocks to Improve the Stability of Metal-Organic Frameworks for Efficient Mercury Removal, *Inorg. Chem.*, 2018, **57**, 6118–6123.

61 J. Li, X. Li, A. Alsaedi, T. Hayat and C. Chen, Synthesis of highly porous inorganic adsorbents derived from metal-organic frameworks and their application in efficient elimination of mercury(II), *J. Colloid Interface Sci.*, 2018, **517**, 61–71.

62 A. Hakimifar and A. Morsali, Urea-Based Metal-Organic Frameworks as High and Fast Adsorbent for Hg²⁺ and Pb²⁺ Removal from Water, *Inorg. Chem.*, 2019, **58**, 180–187.

63 H. Li, H. Liu, J. Zhang, Y. Cheng, C. Zhang, X. Fei and Y. Xian, Platinum Nanoparticle Encapsulated Metal-Organic Frameworks for Colorimetric Measurement and Facile Removal of Mercury(II), *ACS Appl. Mater. Interfaces*, 2017, **9**, 40716–40725.

64 Q. Liu, Q. Zhang, B. Liu and J. Ma, A new synthesis and adsorption mechanism of ZrO₂ based metal-organic frames for efficient removal of mercury ions from aqueous solution, *Ceram. Int.*, 2019, **45**, 15720–15724.

65 Y. Wu, G. Xu, F. Wei, Q. Song, T. Tang, X. Wang and Q. Hu, Determination of Hg(II) in tea and mushroom samples based on metal-organic frameworks as solid phase extraction sorbents, *Microporous Mesoporous Mater.*, 2016, **235**, 204–210.